Drag coefficient prediction of complex-shaped snow particles falling in air beyond the Stokes regime

Giorgia Tagliavini [a,b,*], Mark McCorquodale [d,e], Chris Westbrook [d], Pascal Corso [h], Quirine Krol [f,g], Markus Holzner [b,c]

[a] Institute of Environmental Engineering, Department of Civil, Environmental and Geomatic Engineering, ETH Zürich, Zürich, Switzerland
[b] Swiss Federal Institute for Forest, Snow and Landscape Research, WSL, Birmensdorf, Switzerland
[c] Swiss Federal Institute for Aquatic Science and Technology, Eawag, Dübendorf, Switzerland
[d] Department of Meteorology, University of Reading, Reading, UK
[e] Department of Civil Engineering, University of Nottingham, UK
[f] Swiss Federal Institute for Snow and Avalanche Research, SLF, Davos, Switzerland
[g] Subzero Research Lab, Montana State University, Bozeman, United States
[h] ARTORG Center of Biomedical Engineering Research, Bern, Switzerland

ARTICLE INFO

ABSTRACT

This study considers complex ice particles falling in the atmosphere: predicting the drag of such particles is important for developing of climate models parameterizations. A Delayed-Detached Eddy Simulation model is developed to predict the drag coefficient of snowflakes falling at Reynolds number between 50 and 2200. We first consider the case where the orientation of the particle is known a posteriori, and evaluate our results against laboratory experiments using 3D-printed particles of the same shape, falling at the same Reynolds number. Close agreement is found in cases where the particles fall stably, while a more complex behavior is observed in cases where the flow is unsteady. The second objective of this study is to evaluate methods for estimating the drag coefficient when the orientation of the particles is not known a posteriori. We find that a suitable average of two orientations corresponding to the minimum and maximum eigenvalues of the inertia tensor provides a good estimate of the particle drag coefficient. Meanwhile, existing correlations for the drag on non-spherical particles produce large errors ($\approx$ 50%). A new formula to estimate snow particles settling velocity is also proposed. Our approach provides a framework to investigate the aerodynamics of complex snowflakes and is relevant to other problems that involve the sedimentation of irregular particles in viscous fluids.

1. Introduction

Snow plays a vital role in the climate system. Snowfalls depend on weather conditions and the original form of snow crystals, which are characterized by a wide range of shapes and sizes: from tiny snow crystals (few micrometers) in the upper atmosphere to large snowflakes (up to a few centimeters) near the ground (Kikuchi et al., 2013). Hence, predicting their drag coefficient and falling speed is a crucial step towards the understanding of their falling behavior to constrain parametrizations used in climate models that predict snow precipitations (Newman et al., 2009; Garrett et al., 2012). To study snow crystals motion in the atmosphere, one must rely on the theory of the interaction between a fluid and a particle immersed in it. This interaction depends strongly on object shape, type of fluid and on flow regime (Reynolds number, *Re*), which influence the aerodynamic forces acting on the object.

The motion of spherical and non-spherical particles in the Stokes regime ($Re < 1$, where $Re = (u_t D_{\max})/\nu$, with Re being the particle Reynolds number, u_t the snowflake terminal velocity [m/s], $D_{\max}$ the maximum span of the particle normal to the flow direction [m], and ν the kinematic viscosity of air [m²/s]) has been widely investigated in the past (Brady and Bossis, 1988; Brenner, 1963; Happel and Brenner, 1983; Leith, 1987; Proudman and Pearson, 1957; Stokes, 1851; Oseen, 1927). Notwithstanding this

* Corresponding author at: Institute of Environmental Engineering, Department of Civil, Environmental and Geomatic Engineering, ETH Zürich, Stefano-Franscini-Platz 5, Zürich 8093, Switzerland

E-mail address: tagliavini@ifu.baug.ethz.ch (G. Tagliavini).

extensive research, snow particles cannot be approximated using spheres or ellipsoids without introducing large errors, since their shape irregularities entail much more complexity in their falling motion (McCorquodale and Westbrook, 2020; Zeugin et al., 2020). Furthermore, Stokesian dynamics is valid only for small, single crystals with maximum dimension D_{max} smaller than 100 μm Westbrook (2008), while the majority of snow particles at the ground fall as aggregated crystals with much larger D_{max} Gunn and Marshall (1957), thus outside the Stokes limits. Due to the wide range of sizes (i.e., Reynolds numbers), snow particles may display various falling behaviors that encompass stable ($Re \lesssim 100$) and unstable falling trajectories ($Re \gtrsim 100$), such as periodic (tumbling, oscillating) or chaotic motion (with random rotations around different axes). The types of motions that a particle exhibits at a given Re, as well as the effect this has on C_D, is fairly poorly understood for particles with complex irregular shapes. It is thus difficult to achieve high accuracy in the drag prediction, especially at moderately high particle Reynolds numbers. To overcome this complication and obtain a comprehensive understanding of snowflakes interaction with the surrounding air, both numerical and experimental approaches have been considered, with a major focus on the drag coefficient.

Several attempts have been made to find empirical relations for aerodynamics coefficients of non-spherical particles within and beyond the Stokes regime. Sanjeevi et al. (2018) studied the drag, lift and torque coefficients and their dependency, not only on the Reynolds number, but also on particle orientation, building on the work of Leith (1987), which focused on the Stokes regime only. They proposed new formulas to evaluate the drag, lift and torque coefficients for non-spherical particles (namely disks, ellipsoids, and fibers) as a function of the angle of incidence ϕ ($0° < \phi < 90°$) and shape coefficients for Re up to 2000. These relations derive from a series of fluid dynamics simulations of fixed particles at different angles of incidence performed with the Lattice Boltzmann method. The results were compared with the experimental ones from Hölzer and Sommerfeld (2008); Zastawny et al. (2012), and Ouchene et al. (2016) extended up to $Re = 2000$. While Sanjeevi et al. (2018) and Zastawny et al. (2012) used shape coefficients for their empirical relations of aerodynamic coefficients, Hölzer and Sommerfeld (2008) made use of the sphericity Φ (ratio between the surface area of the volume equivalent sphere and that of the considered particle) to describe non-spherical geometries. More complex shape factors were employed by Bagheri and Bonadonna (2016); Tran-Cong et al. (2004) and Binder et al. (2006) to model the drag coefficient of volcanic particles and aggregates of spheres, respectively. These studies represent only a first step towards a better prediction of complex-shaped particles aerodynamic coefficients. In that, the analyzed particles and aggregates are rather simple (ellipsoid, fibers or aggregates of spheres), while snow particles present more elaborate shapes. Additionally, the relation obtained for the aerodynamic coefficients are generally empirical and not related to a physical behavior, ergo the applicability beyond the specific cases remains uncertain.

Since the early 50s, experimental approaches have been used by the atmospheric sciences community to built mathematical relations for the drag coefficient and settling velocity of different shapes of snowflakes and snow aggregates. Langleben (1954) and Magono and Nakamura (1965) found that the terminal velocity (u_t) of snow crystals is dependent on the shape and mass (or density) of the particle and proposed a power-law to predict it. Heymsfield and Westbrook (2010) proposed a new equation for u_t based on the area ratio A_R (ratio between the projected area of the snow crystal and the frontal area of the circumscribed disk) together with a relation between Reynolds and Best numbers (defined as $X = C_D Re^2$, where X is the Best num-

ber) and compared it to limited experimental data, finding errors lower than 25%. The works of Mitchell and Heymsfield (2005) and Heymsfield and Westbrook (2010) were compared in the paper by Westbrook and Sephton (2017), in which terminal velocities of 3D-printed snowflakes falling in a mixture of glycerine and water were recorded, showing a discrepancy in the final speeds of $\approx 80\%$ from Mitchell and Heymsfield (2005) and $\approx 45\%$ from Heymsfield and Westbrook (2010). Preferential orientations of different snow crystals geometries were also investigated up to $Re \approx 1000$ in the same paper.

As far as computational models are concerned, fall attitudes of simple shapes, such as spheres, disks, hexagonal ice-plates, and columnar crystals Uhlmann and Dusek (2014); Auguste et al. (2013); Cheng et al. (2015); Hashino et al. (2016) are usually investigated at low and moderate Reynolds numbers. In this context, Direct Numerical Simulation using the Immersed Boundary Method Uhlmann and Dusek (2014) or grid-adapting solutions with 6DoF (degrees of freedom) solvers Cheng et al. (2015) are generally employed. These are good solutions to investigate complex particle trajectories, but such models become unnecessarily expensive in terms of computational resources if used with the only aim of drag coefficient prediction. In these works, forces and torques acting on the particles together with the wake structures and vorticity are taken into account. Falling behavior is also investigated, although the falling trajectories are restricted to stable or mildly unstable (oscillatory) motion, due to limitations in the Reynolds number range.

The empirical relations available in the literature for drag coefficient and terminal velocity have a comprehensive purpose, but are usually limited by fitting parameters, which are restrained to specific experimental set-ups and their related errors. On the contrary, numerical models can give a more accurate prediction, however very few studies have been published so far on more complex snow crystals or aggregates. For instance, the recent work of Zeugin et al. (2020) investigated realistic snow particles in the Stokes regime and proposed sphericity-based relations to estimate aerodynamic coefficients and the settling velocity of such particles up to $Re \approx 10$. Therefore, a more systematic approach to determine the drag coefficient of irregular particles for a broader range of Reynolds numbers is needed and that is exactly the purpose of this paper.

The first objective of this work is to present a Delayed-Detached Eddy Simulation (DDES) model to predict the drag coefficient of complex-shaped snow particles in air (within a Reynolds number range of $50 \lesssim Re \lesssim 2200$, i.e., ice particle size of roughly several hundred microns to several centimeters) when the orientations that the particles adopt in free-fall are known a posteriori (Section 3.1). That is, in the DDES model we investigate particles fixed in the same orientation that we observed in laboratory experiments in which 3D-printed particles of the same geometric shape fell in a fluid at rest (see Sections 2.1 and 2.1.1). The fixed orientation of the particle in the DDES model corresponds to the orientation observed in the laboratory experiments when the particles fell steadily (at low Reynolds number), which we refer to as the "final orientation and which serves as an "average final orientation" also for moderate and high Reynolds numbers. This approach is validated by comparing the results from different LES and DDES (hybrid URANS-LES) approaches with experimental data. A grid convergence study is also performed.

The second objective of this work is to propose a new approach to accurately estimate the drag coefficient of snow crystals when the orientation that the particle adopts in free-fall is not known a posteriori (Section 3.2). This approach entails simulating snowflakes at two different orientations described by the maximum and minimum eigenvalues of their inertia tensor. For this purpose, a computational model is built, in which the airflow

around a fixed, single snow particle is solved. To save computational time and, at the same time, preserve accuracy, the same DDES approach is employed to model the airflow as we used in the final orientation model. The accuracy of this approach is also evaluated by comparing the results with data from the laboratory experiments. Ultimately, we provide an estimate of the snow particle settling velocity based upon geometrical information from the inertia tensor and experimental observations.

We stress that both sets of simulations reported here are carried out with an open source code (OpenFoam), and thus are accessible to a broad spectrum of users (which is not the case for most of DNS codes). In addition, the work presented in this paper will be a valuable tool to estimate the drag coefficient of an irregular particle, regardless the availability of a posteriori knowledge of the kinematics of the particle in free-fall. We anticipate that the presented model can also be used as the basis for the development of more complex models to investigate particle-fluid interactions in a much broader range of applications.

2. Materials and methods

2.1. Experimental set-up and final orientation reconstruction

A series of laboratory experiments were conducted in which the motion of 3D-printed models of ice particles was recorded as the particles fell in fluids at rest. In order to include complex-shaped particles within the study, 3D-printed analogs (density of 1174 kg/m^3) were manufactured at a scaled-up size (typically 10–20 mm in size) and dropped in a tank containing viscous liquids; this ensured that the particles fell at the same Reynolds numbers as ice particles falling in the atmosphere. In these experiments, the tank was filled with uniform mixtures of water and glycerol, in which the volume fraction of glycerol was set between 0 and approximately 50% (density between 999 kg/m^3 and 1144 kg/m^3).

The trajectory of falling analogs was recorded over a region approximately 0.2 m × 0.2 m × 0.2 m in size using a system of three synchronized cameras positioned to have orthogonal views of the tank. An algorithm (the Trajectory Reconstruction Algorithm implemented through Image anaLysis, TRAIL) was used to reconstruct the time-resolved trajectory and orientation of falling analogs over the recorded region. Using this system, the trajectories of 3D-printed analogs were reconstructed to an accuracy of better than ± 0.5 mm, whilst the orientation of the falling analogs was reconstructed to an accuracy of ±2.5°. The data generated by the algorithm enables the determination of *Re* and C_D to within an estimated accuracy of approximately 5% and 7%, respectively. Moreover, the data generated by the algorithm permits more complex analyses of the observed motion. For example, the detailed reconstructions generated using TRAIL facilitates the export of data describing the precise orientation of falling particles across a series of time steps. In other words, the shape of a particle is represented by a series of triangular facets within the TRIAL algorithm. The digital reconstruction created using the TRAIL algorithm describes the location of the facets representing the particle surface, such that it is possible to export data describing the particle orientation in a format (stereolithography (STL) files) that could be readily incorporated into the numerical model described in Section 2.2. The experimental approach exploits dynamic similarity; when falling steadily the aerodynamics of ice particles is a function of only the geometric shape of the particles and the Reynolds number at which they fall List and Schemenauer (1971). Consequently, when falling steadily, relationships between dimensionless quantities, such as the *Re* and C_D, are the same for ice particle analogs falling in viscous liquids and natural ice particles falling in the atmosphere.

Full details of the experiments used to validate the current work, including a detailed description of the experimental procedure and a summary of drag coefficient measurements, are reported separately by McCorquodale and Westbrook (2020a,b).

2.1.1. Steady and unsteady motion of falling snow particles

Snow particles can be found in nature in many shapes and sizes (Kikuchi et al., 2013). The snow particle shapes incorporated in this work are shown in Fig. 1 and are chosen such that they comprise the snowflakes classes that are most com-
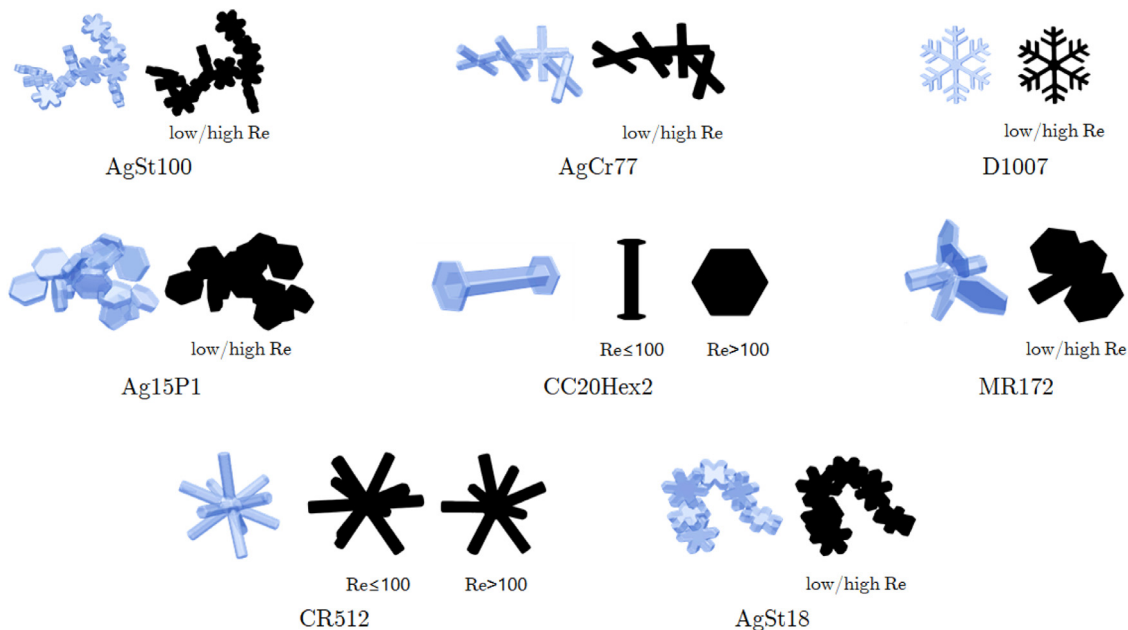

Fig. 1. 3D geometries of the different snow particles taken into account in this paper (in blue). They are illustrative of the four main categories of snow particles observed in nature: aggregates (*AgSt100, AgCr77, Ag15P1,* and *AgSt18*), rosette crystals (*MR172* and *CR512*), capped-column crystal (*CC20Hex2*), and plate-like crystals (*D1007*). *AgSt100* is used for the validation. Beside each geometry, their projection in the flow direction *x* (according to the final orientation reconstruction) is shown for different flow regimes (in black). The names of the geometries are chosen to facilitate the comparison to the extensive data reported in the supplementary material of McCorquodale and Westbrook (2020). (For interpretation of the references to color in this figure legend, the reader is referred to the web version of this article.)
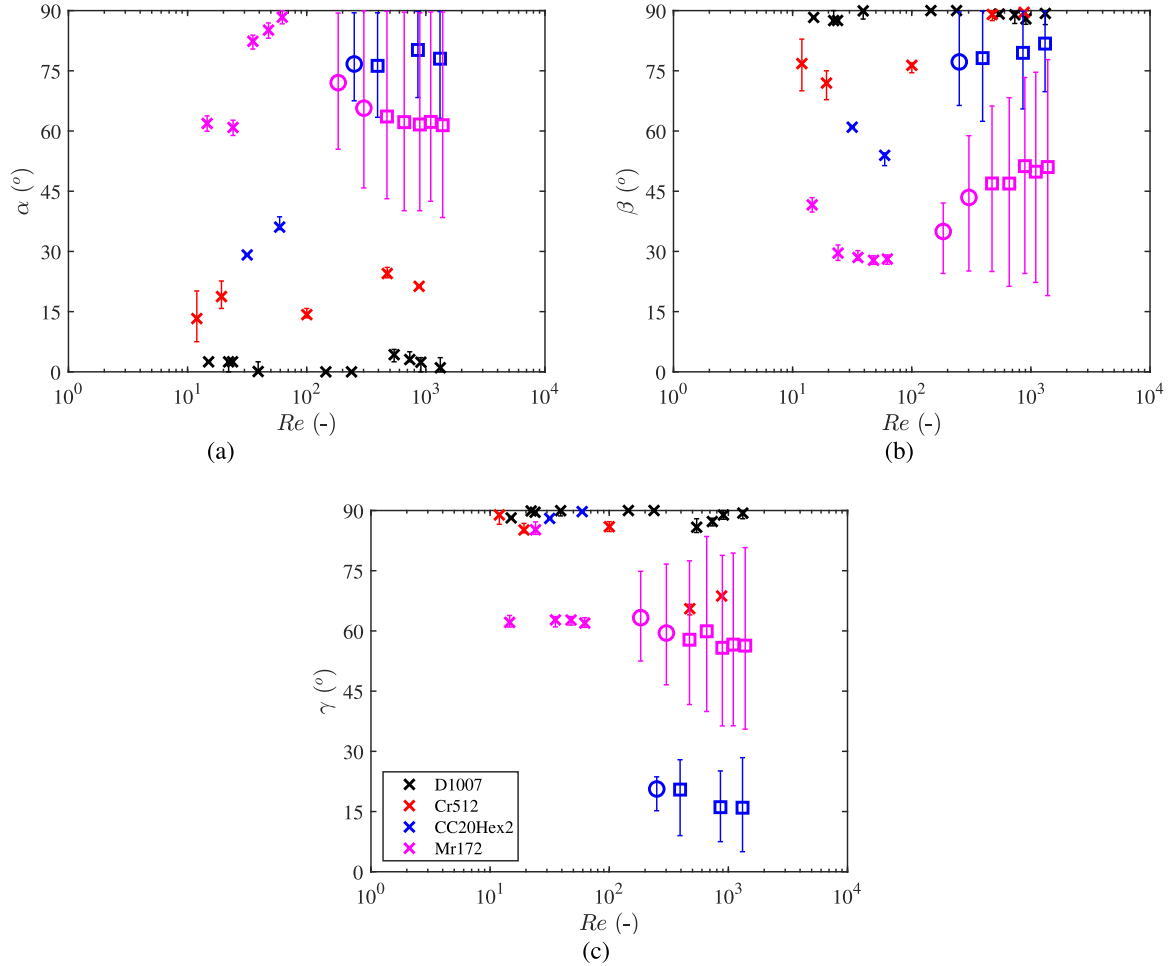
Fig. 2. Time-averaged measurements of the angle between the principal axes and the fall direction for the particles *D1007, CR512, CC20Hex2*, and *MR172* (see legend in panel (c), which applies to all plots); (a) largest principal axis, (b) intermediate principal axis and (c) the smallest principal axis. Error bars show the range in orientations observed as particles traveled through the measurement region, either as a result of measurement uncertainty (small, ≈ 2.5°) or where particles were observed to fall unsteadily (e.g., *MR172* and *CC20Hex2*). Different symbols are used to distinguish between particles that were observed to fall steadily (×) and those that were observed to exhibit periodic (○) or chaotic (□) motions as they fell.

mon in nature: plate-like crystals (*D1007*), rosette particles (*MR172* and *CR512*), capped-column crystals (*CC20Hex2*), and aggregates (*AgSt100, AgCr77, Ag15P1*, and *AgSt18*). The names of the snowflakes are chosen to facilitate the comparison to the extensive data reported in the supplemental material of McCorquodale and Westbrook (2020), which includes data on the particle geometries used in this study. We stress that these snowflakes have distinct geometries and as a consequence these particles were observed to exhibit distinct falling motions during the experiments described in Section 2.1. A summary of the motions observed in the experiments is shown in Figs. 2 and 3, in which we have plotted data describing the orientation that each particle was observed to adopt in free-fall at a range of Reynolds numbers.

During experiments, the plate-like crystal *D1007* fell steadily across an extensive Reynolds number range (10 ≲ *Re* ≲ 1500), and adopted an orientation broad-side onto the flow (i.e., with the maximum principal moment of inertia aligned parallel to the fall direction) as shown in Fig. 1 and 2. That is, the particle fell steadily with an orientation like that adopted by simple circular discs, although steady falling motions were observed to occur at Reynolds numbers an order of magnitude larger than observed for circular discs (Field et al., 1997). Likewise, the rosette *CR512* was also observed to fall steadily across an extensive Reynolds number range (10 ≲ *Re* ≲ 1000). However, a modest change in orientation

that the particle adopted in free-fall was observed at *Re* ≈ 10², as shown in Figs. 1 and 2.

In contrast, the remaining particles were observed to present a more complex range in motions as they fell at different Reynolds numbers. For example, the rosette *MR172* was only observed to fall steadily with a stable orientation for *Re* ≲ 100; for *Re* ≳ 100 the particles were observed to exhibit large-amplitude oscillations as they fell, as shown in Fig. 2. Initially, the reconstructed traces of displacement and particle orientation corresponding to the oscillations were periodical, but as *Re* increased the oscillations became chaotic. Likewise, a distinct change in the observed motion of the capped-column *CC20Hex2* was observed at *Re* ≈ 100. For *Re* ≲ 100 the capped column was observed to fall steadily with its long-axis aligned perpendicular to the fall direction (i.e., with the smallest principal moment of inertia aligned perpendicular to the fall direction) as shown in Figs. 1 and 2. However, for *Re* ≳ 100 the capped columns exhibited helical motions, whereby the long-axis of the particle was approximately aligned parallel to the fall direction. A pair of rigidly linked discs exhibited similar behavior, as reported by Kim et al. (2018). Initially, the helical motions exhibited clear periodicity, but as *Re* increased the helical motions became irregular and the observed motion was chaotic.

The more irregularly-shaped aggregate snowflakes (*AgSt100, AgCr77, Ag15P1*, and *AgSt18*) also exhibited different motions in
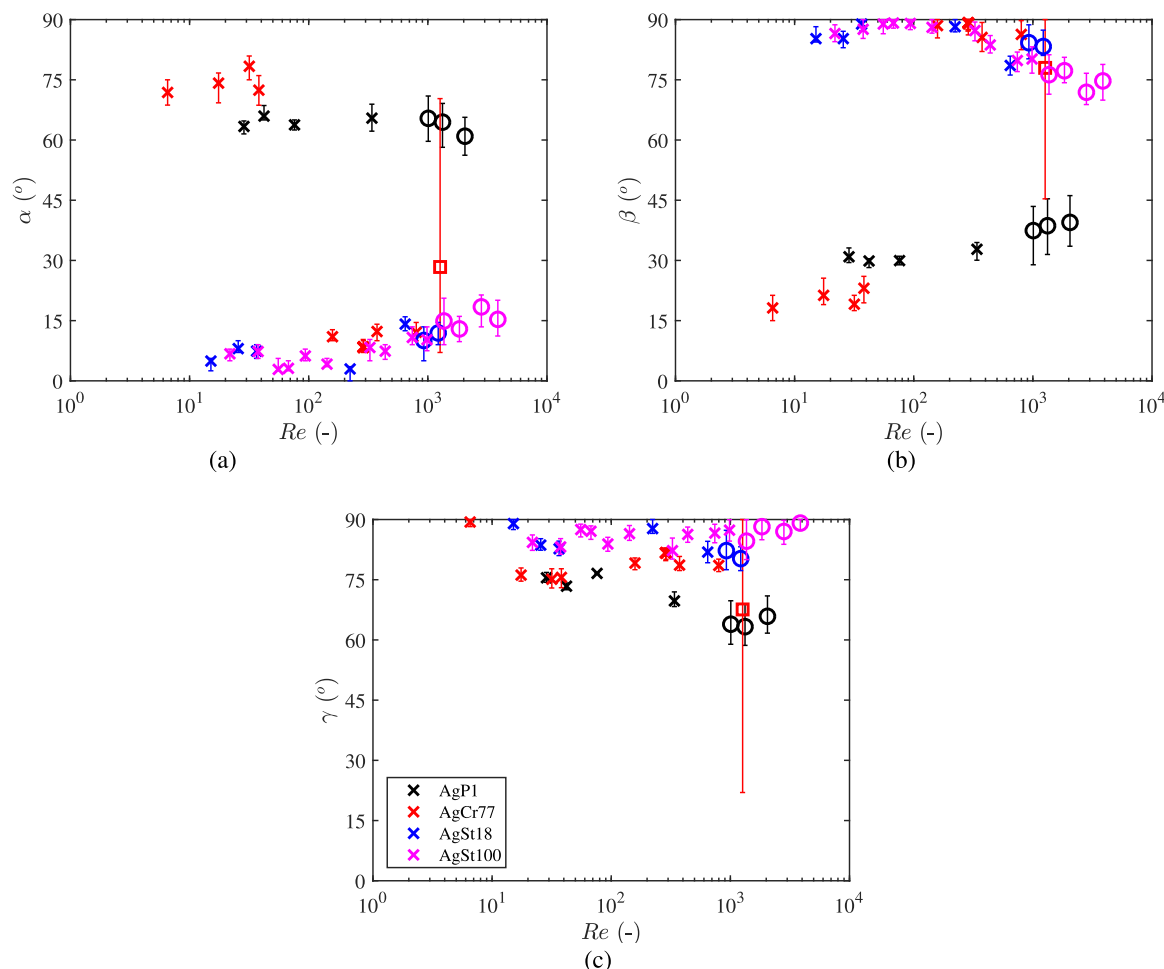
Fig. 3. Time-averaged measurements of the angle between the principal axes and the fall direction for the particles *Ag15P1, AgCr77, AgSt18,* and *AgSt100* (see legend in panel (c), which applies to all plots); (a) largest principal axis, (b) intermediate principal axis and (c) the smallest principal axis. Error bars show the range in orientations observed as particles traveled through the measurement region, either as a result of measurement uncertainty or where particles were observed to fall unsteadily. Different symbols are used to distinguish between particles that were observed to fall steadily ($\times$) and those that were observed to exhibit periodic ($\circ$) or chaotic ($\square$) motions as they fell.

free-fall. At low Reynolds number ($Re \lesssim 10^3$), particles were observed to fall steadily with a stable orientation but exhibited a spiraling trajectory, whereby the particles rotated around a (vertical) axis aligned with the fall direction. The spiraling trajectories observed were a result of a constant rotation of the particles due to the center of mass and center of drag not being co-located (McCorquodale and Westbrook, 2020). Within this regime, *AgSt100, Ag15P1,* and *AgSt18* were observed to display only modest changes in orientation as the Reynolds number increased, as shown in Fig. 3. However, a distinct change in orientation was observed to occur for *AgCr77* at $Re \approx 100$. At higher Reynolds number (the threshold is different for each particle) the snowflake particles were again observed to fall in spiraling trajectories, but (periodic) small amplitude fluttering motions were observed to occur, as shown in Fig. 3. However, Fig. 3 also shows that much larger amplitude fluttering motions were observed for *AgCr77* at $Re \approx 1200$; in this case the fluttering motions were irregular and the motion of the particle was chaotic. The origin of the differences in motions observed for *AgCr77* relative to *AgSt100, Ag15P1,* and *AgSt18* is currently unclear.

The Reynolds numbers and the observed orientations are used to inform the computation model, providing the inflow velocity and the particle orientation with respect to the flow direction, as described in Sections 2.2 and 2.2.1. Fig. 1 shows the orientation of each snow particle used within the final orientation numerical model. This orientation corresponds to the one observed in a single experiment where the particle was falling steadily. The position that particles adopt when falling steadily are also used in the final orientation numerical model for cases in which particles were observed in the experiments to fall unsteadily (i.e., at high Reynolds number). This is a reasonably good assumption for most particles, since the low Reynolds number orientation lies within the range of the orientations recorded when the particles fall unsteadily. However, in Section 4, we show evidence that for certain particles, at high Re, the drag in this assumed orientation can be radically different to the actual value experienced by the particle as it undergoes complex unsteady motions.

2.2. Numerical model and convergence studies

The computational model presented in this work solves for the fluid domain, where a realistic snow particle is accounted for as a fixed object impinged by the airflow. The model geometry and sizes are shown in Fig. 4 and are based on best practice guidelines for computational fluid dynamics (Franke et al., 2007). Both domain size and grid convergence studies are performed to assess the domain dimensions and its spatial discretization errors by means of Richardson extrapolation (Roache, 1994). As far as the domain size convergence study is concerned, three different dimensions are tested: the actual size and other two with halved and doubled dimensions, respectively. The domain is shown in Fig. 4 and
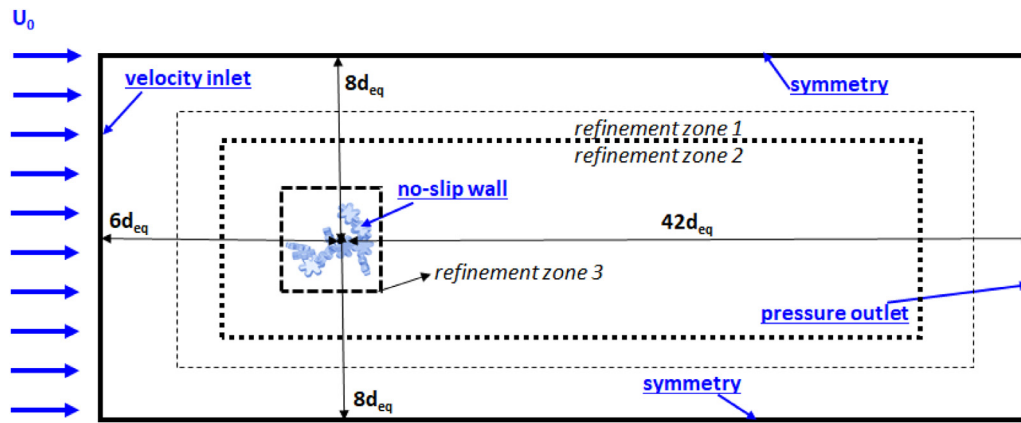
Fig. 4. Computational domain size as a function of volume-equivalent sphere diameter (d_{eq}) and boundary conditions. This set-up is valid for all the simulations performed in this work.
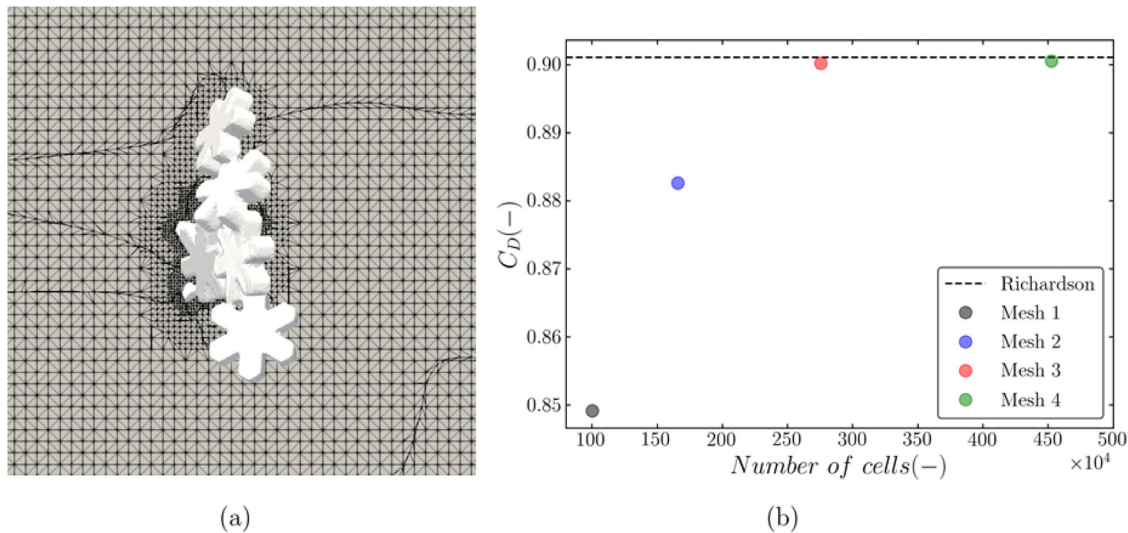

Fig. 5. (a) Mesh detail of the refinement zone close to the snowflake surface for particle *AgSt100* (validation case). (b) Results from the grid convergence analysis with four different grid sizes (Total number of cells: *Mesh 1* = 1.00×10^6, *Mesh 2* = 1.67×10^6, *Mesh 3* = 2.78×10^6, and *Mesh 4* = 4.64×10^6).

the results of the size convergence analysis can be found in the Supplementary Material (Figure A). For the grid convergence study, the model set-up is the same as the validation case described in Sections 2.2.1 and 2.2.2. Four different grids with an increasing number of cells (factor of 0.6) are tested and, for each of them, the drag coefficient is calculated using Eq. (4). It emerges that the minimum number of grid cells must be larger than $\backsim 3.0 \times 10^6$ (resulting in an error of $\approx 0.10\%$) to preserve model accuracy (Fig. 5(b)). The final unstructured grid is composed of a hexagonal base mesh and three refinement zones with triangular elements. The first two refinement zones cover the air domain upstream and downstream of the snow particle, and the third one comprises the fluid domain in the proximity of the snowflake. For the latter, the refinement layers are built such that they reproduce a boundary layer mesh and the thickness of the first layer is chosen to have $y^+ \approx 1$ (dimensionless wall distance based on friction velocity and kinematic viscosity) in the wall-adjacent cells (Fig. 5(a)), obtaining a minimum element size of $\approx 3.2 \times 10^{-5}$ m and a maximum cell size of $\approx 7.6 \times 10^{-3}$ m. The grid is generated using the OpenFOAM utility *snappyHexMesh* OpenFOAM (2017). The total number of grid cells slightly varies ($\pm 5\%$) for each snowflake. This is due to the dissimilar snow particle shapes, which influence the cells generation especially of the refinement zone in the proximity of the particle. The mesh features, together with the outcome of the conver-

gence analysis are shown in Fig. 5. The domain size and grid convergence study, together with the model validation are performed using particle *AgSt100* (Fig. 1), while a subset of the particle geometries used by McCorquodale and Westbrook, 2020 is employed for the remaining simulations, as illustrated in Fig. 1.

To keep the domain size constant, Reynolds similarity is used to match the conditions of the laboratory experiments (described in Section 2.1) used to validate the computational model. That is, the volume of each snowflake is arbitrarily scaled to be equal to that of a sphere with a diameter of 1 cm (i.e., volume-equivalent sphere), which is positioned with its center of mass at the coordinate center (see Fig. 4), whilst a (uniform) air speed that satisfies Reynolds similarity is imposed at the inlet. The uniform air speed is calculated from:

$$u_\infty = \frac{Re \; \nu}{D_{\max}}, \tag{1}$$

where Re is the desired particle Reynolds number (a set of Reynolds numbers for each snow particle is provided from experimental data (see Table 2)), $D_{\max}$ is the maximum dimension of the snow particle (normal to the flow direction) in [m], u_∞ is the uniform inlet velocity in [m/s] and ν is the kinematic viscosity of the fluid [m²/s]. In the experiments, the choice of $D_{\max}$ as characteristic length for the Reynolds number was based not on a rigorous, physical justification, but on practical reasons. That is, in-

Table 1

Data from the turbulence models validation for snow particle *AgSt100* (Section 2.2, Fig. 1). The values obtained from the experiments described in Section 2.1 are compared with the simulations, and the drag prediction for each Reynolds number is shown. The area ratio measured during experiment slightly changes due to the motion of the particle. For the model a fixed area ratio ($A_R = 0.37$) is considered by averaging the experimental values. The error is evaluated using Eq. (10). Furthermore, the averaged absolute error is evaluated and the falling behavior observed during the experiments is reported (S = stable, P = periodic, C = chaotic).

Turbulence model	Area ratio	Density	Kinematic viscosity	Re	C_D experiments	Falling behavior	C_D simulations	Error C_D%
	0.37	1144	8.63×10^{-6}	38	3.10	S	3.31	6.32
	0.36	1144	8.71×10^{-6}	144	1.76	S	1.92	8.43
	0.38	999	1.12×10^{-6}	1366	0.93	P	1.02	8.29
AgSt100	0.38	999	1.14×10^{-6}	2815	0.89	P	0.93	5.22
	0.38	999	1.13×10^{-6}	3868	0.94	P	0.90	−4.13
DDES							**averaged absolute error**	6.48
	0.37	1144	8.63×10^{-6}	38	3.10	S	3.36	7.78
	0.36	1144	8.71×10^{-6}	144	1.76	S	1.93	8.78
	0.38	999	1.12×10^{-6}	1366	0.93	P	1.02	8.83
AgSt100	0.38	999	1.14×10^{-6}	2815	0.89	P	0.94	5.52
	0.38	999	1.13×10^{-6}	3868	0.94	P	0.90	−3.95
WALE							**averaged absolute error**	6.98
	0.37	1144	8.63×10^{-6}	38	3.10	S	3.48	10.79
	0.36	1144	8.71×10^{-6}	144	1.76	S	1.93	8.95
	0.38	999	1.12×10^{-6}	1366	0.93	P	1.05	10.99
AgSt100	0.38	999	1.14×10^{-6}	2815	0.89	P	0.95	6.33
	0.38	999	1.13×10^{-6}	3868	0.94	P	0.90	−3.92
Smagorinsky							**averaged absolute error**	8.20

strumentation used to obtain measurements of natural ice particles typically provides very limited geometric information about the particles. However, the maximum dimension of an ice particle in the flow (or fall) direction can be easily and accurately measured using a wide range of meteorological instrumentation (Garrett et al., 2012; Newman et al., 2009; Schönhuber et al., 2007). For this reason, D_{max} is commonly utilized as the characteristic length for the Reynolds number of natural ice particles in meteorological applications. Moreover, due to the high variability of the snowflakes shapes Kikuchi et al. (2013), it is difficult to conceive an alternative geometrical quantity that can be used to characterize the shape of natural ice particles that is both simple to measure and that can be directly linked to the structure of wake of the particles. Therefore, the "conventional" approach is also followed in the model. At the outlet, a zero static pressure is established. The snowflake is treated as a fixed wall on which a no-slip condition with zero roughness is set, and the symmetry boundary condition is set for the lateral boundaries of the flow domain (Fig. 4). For the model validation (Section 2.2.2), we match the fluid properties (water-glycerin mixture) of the experiments within the flow domain (Table 1) to accurately reproduce the laboratory conditions. The remaining case studies employ air properties at 0 °C and atmospheric pressure at sea level ($\rho = 1.29$ kg/m^3, $\nu = 1.33 \times 10^{-5}$ m^2/s) instead, to avoid changing the density for each Reynolds number, as shown in Table 1 for the validation case. We match the Reynolds numbers of the experiments for all the case studies presented in this paper.

2.2.1. Governing equations and numerical simulations

The computational model is built up with Open source Field Operation and Manipulation (OpenFOAM 4.1) C++ software based on the finite volume method. In the model, the air flow motion is attained by solving the transient Navier-Stokes equations:

$$\nabla \cdot \boldsymbol{u} = 0,$$
$$\rho \left(\tfrac{\partial \boldsymbol{u}}{\partial t} + (\boldsymbol{u} \cdot \nabla) \boldsymbol{u} \right) = -\nabla p + \mu \nabla^2 \boldsymbol{u} + \rho \boldsymbol{f}, \tag{2}$$

in which $\boldsymbol{u}$ is the flow velocity [m/s], ρ is the fluid density in [kg/m^3], p the pressure in [Pa], μ is the dynamic viscosity of the fluid in [Pa s] and $\boldsymbol{f}$ are any external forces per unit mass [N/kg]. The interaction between the air and the snow particle is described through Newton's second law of motion. The forces generated by the flow impinging the snowflake comprise normal pressure and tangential viscous contributions:

$$\boldsymbol{F} = \boldsymbol{F}_p + \boldsymbol{F}_\nu = \int_A p\boldsymbol{n}dA + \int_A \tau \cdot \boldsymbol{n}dA, \tag{3}$$

where $\boldsymbol{n}$ is the normal and tangential unit vector on the particle surface A and τ represents the viscous stresses [Pa]. The turbulence modeling and validation are described in Section 2.2.2.

The transient flow problem is discretized using second-order, central-difference schemes. In particular, a second-order backward-differencing time-stepping scheme is chosen for the first-order time derivative term in Eq. (2), for it is a second-order, conditionally stable scheme. Furthermore, for the divergence term of the velocity in Eq. (2) the Linear-Upwind Stabilized Transport (LUST) is employed, in which the linear-upwind scheme is blended with linear interpolation to stabilize the solution while maintaining a second-order behavior. For all the selected schemes, the cell limiting option is also included to bound the extrapolated cell value to the one of the surrounding cells in the gradient scheme, while divergence schemes are bounded to help to maintain boundedness of the solution and promoting better convergence. This is a second-order, implicit scheme and conditionally stable OpenFOAM (2017).

With regard to the transient solver employed in the numerical model, for each Reynolds number, the time step is selected such that it fulfills the condition of $CFL = (u_\infty \triangle t)/(\triangle x) \le 1$ (where $\triangle t$ is the time step [s] and $\triangle x$ is the grid spacing [m]), the time discretization being implicit. Each simulation runs for 20,000 time steps to obtain a fully developed wake behind the snow particle, following the rule of thumb of minimum 5 flow through times (i.e., the time needed for the flow to enter and exit the domain at the inlet velocity set as boundary condition) Durbin and Medic (2007). The PIMPLE algorithm is used for computing the solution. It is a combination of PISO (Pressure Implicit with Splitting of Operator) and SIMPLE (Semi-Implicit Method for Pressure-Linked Equations) Ferziger and Perić (2002); OpenFOAM (2017). All these algorithms are iterative solvers, but PISO and PIMPLE are both used for transient cases, whilst SIMPLE is used for steady-state cases. The PIMPLE algorithm works as the SIMPLE algorithm for each time step, where outer correctors set the number of iterations and, once converged, will move on to the next time step until the solution is complete. Better stability is obtained from PIMPLE over PISO for this reason, especially when dealing with large time steps or when the nature of the solution is inherently unstable. The number of

Table 2

Summary of the comparison between model and experiments for snow particles at their final orientation (Section 2.2, Fig. 1). The error is evaluated using Eq. (10). The falling behavior observed in the experiments is also highlighted (S = stable, P = periodic, C = chaotic).

Particle name	Re	C_D experiments	Falling behavior	C_D simulations	Error C_D %
AgCr77 ($A_R = 0.21$)	158	1.92	S	1.95	1.74
	287	1.42	S	1.52	6.93
	799	1.01	S	1.07	5.49
	1254	0.96	P	0.96	0.74
	1314	0.94	P	0.95	1.16
				averaged absolute error	3.21
D1007 ($A_R = 0.37$)	145	2.95	S	3.01	2.11
	542	1.92	S	1.95	1.78
	909	1.69	S	1.66	−1.81
	1322	1.57	S	1.49	−5.30
				averaged absolute error	2.75
Ag15P1 ($A_R = 0.47$)	77	1.59	S	1.63	1.05
	1009	0.81	P	0.75	−8.79
	1327	0.81	P	0.74	−9.65
	2049	0.81	P	0.73	−10.60
				averaged absolute error	7.52
CC20Hex2 ($A_R = 0.52$)	59	2.81	S	3.02	6.95
	251	1.08	P	1.63	33.56
	393	1.05	C	1.61	34.65
	858	1.00	C	1.69	40.63
	1315	1.01	C	1.65	38.68
				averaged absolute error	30.98
CR512 ($A_R = 0.39$)	100	1.77	S	1.81	2.18
	297	1.24	S	1.14	−8.79
	475	0.99	S	0.95	−4.30
	878	0.88	S	0.84	−5.10
				averaged absolute error	5.09
MR172 ($A_R = 0.58$)	62	1.72	S	1.83	6.11
	184	1.36	P	1.55	12.59
	472	1.37	C	0.97	−40.32
	890	1.37	C	0.92	−48.77
	1385	1.38	C	0.92	−49.74
				averaged absolute error	31.50
AgSt18 ($A_R = 0.48$)	223	1.23	S	1.36	6.73
	646	1.02	S	1.12	8.82
	926	0.96	P	1.00	4.09
	1222	0.94	P	1.00	6.26
				averaged absolute error	6.48

outer correctors of the PIMPLE algorithm defines how many times the system of equations is solved before it is forced to move onto the next time step, regardless of whether that time step has converged or not. The criterion for time step convergence is defined as the absolute tolerance of the solver, which is set to 1×10^{-8} for the described model Moukalled et al. (2016).

The first part of this work concerns a set of simulations to predict the drag coefficient of real snow particles at their final falling orientation. To this purpose, instantaneous forces acting on the particle are calculated and stored at each time step. Once the calculation is done, the drag force is averaged over time, considering only the last 10,000 time steps, out of the total 20,000 iterations, to avoid taking into account initial flow instabilities (see Supplementary Material, Figure B). From the average drag force, the drag coefficient is evaluated with the following formula:

$$\langle C_D \rangle = \frac{\langle F_D \rangle}{\frac{1}{2}\rho u_\infty^2 A_f}, \tag{4}$$

where $\langle C_D \rangle$ and $\langle F_D \rangle$ are the time-averaged drag coefficient and force, respectively, and A_f is the frontal (or projected) area of the snow particle in the flow direction. It is directly evaluated by averaging the area ratio A_R given in the experimental data set (i.e., the ratio between the projected area of the particle and the cross-sectional area of a sphere with its diameter equal to the maximum dimension of the particle (D_{max}), in a plane orthogonal to the flow direction):

$$A_f = \left(\frac{D_{max}}{2}\right)^2 \pi A_R. \tag{5}$$

The second set of simulations accounts for when the particle final orientation is not known a posteriori. In this view, a new approach to estimate the drag coefficient is presented. Firstly, four snow particles are selected from the geometries in Fig. 1 to test this new approach. Namely, aggregates (*AgCr77* and *Ag15P1*), rosette (*MR172*), and capped-column crystals (*CC20Hex2*) are chosen to include particles that exhibited both periodic and chaotic motion during free-fall experiments (Section 2.1.1). Based on the STL files of each shape, the principal axes are calculated using the *Trimesh* Python library (Dawson-Haggerty et al., 2019). It is then possible to calculate the maximum and the minimum principal moment of inertia, from which we obtain two correspondent projected areas of the particle. Subsequently, for each case listed in Table 3, two different simulations (one for each projected area facing the flow direction) are set up and solved. Following the same methodology described above, the time-averaged drag coefficient for each case is evaluated:

$$\langle C_{D,\min} \rangle = \frac{\langle F_{D,\min} \rangle}{\frac{1}{2}\rho u_{\infty,\min}^2 A_{f,\min}} \quad , \quad \langle C_{D,\max} \rangle = \frac{\langle F_{D,\max} \rangle}{\frac{1}{2}\rho u_{\infty,\max}^2 A_{f,\max}}, \tag{6}$$

in which the subscript max and min stand for the projected areas of maximum and minimum principal moment of inertia, respec-

Table 3

Summarized prediction errors and averaged absolute errors for the geometries tested with the mean drag approach. The comparison between final orientation models, arithmetic, geometric and harmonic mean and experimental data is also shown. The falling behavior observed in the experiments is also highlighted (S = stable, P = periodic, C = chaotic).

Particle	Reynolds number	Falling behavior	Error [%]			
			Final orientation	Arithmetic mean	Geometric mean	Harmonic mean
AgCr77 ($A_R = 0.21$)	158	S	1.74	2.46	1.70	0.94
	799	S	5.49	1.03	0.92	0.81
	1314	P	1.16	1.92	1.92	1.91
	averaged absolute error		2.80	1.81	1.51	1.22
Ag15P1 ($A_R = 0.47$)	77	S	1.05	3.86	3.83	3.81
	1009	P	−8.79	5.40	5.40	5.39
	2049	P	−10.60	−4.24	−4.24	−4.25
	averaged absolute error		6.81	4.50	4.49	4.48
CC20Hex2 ($A_R = 0.52$)	251	P	33.56	13.94	9.69	5.23
	858	C	40.63	16.10	7.87	−1.16
	1315	C	38.68	12.18	2.62	−7.98
	averaged absolute error		37.76	14.07	6.73	4.79
MR172 ($A_R = 0.58$)	472	C	−40.32	9.10	4.68	0.05
	890	C	−48.77	−4.82	−7.17	−9.56
	1385	C	−49.74	−8.47	−10.57	−12.70
	averaged absolute error		46.28	7.47	7.47	7.44

tively. After obtaining the drag coefficients, the arithmetic mean

$$\overline{C_{Darithm}} = \frac{\langle C_{D,\min}\rangle + \langle C_{D,\max}\rangle}{2}, \tag{7}$$

the geometric mean

$$\overline{C_{Dgeom}} = \sqrt[2]{\langle C_{D,\min}\rangle \langle C_{D,\max}\rangle}, \tag{8}$$

and the harmonic mean

$$\overline{C_{Dharm}} = \frac{2\langle C_{D,\min}\rangle \langle C_{D,\max}\rangle}{\langle C_{D,\min}\rangle + \langle C_{D,\max}\rangle}, \tag{9}$$

are evaluated and compared with experimental data. The latter are the three most used types of means to estimate the central tendency (average or mean) of a data set. The arithmetic mean works well with data in an additive (or "linear") relationship and tends to a higher value of the central tendency compared to the geometric and harmonic means. The geometric (which uses a multiplicative relationship) is generally employed for non-linear data sets because it handles varying proportion with ease. Nonetheless, it tends to give a mean that is larger than the harmonic formula, which uses reciprocals and thus leans towards smaller values in the data set. In both set-ups (final orientation and maximum/minimum projected areas) the percentage error of the prediction is assessed (see Table 3) against the experimental data as:

$$\varepsilon = \frac{\langle C_{D,sim}\rangle - \langle C_{D,exp}\rangle}{\langle C_{D,sim}\rangle} \cdot 100. \tag{10}$$

In the final part of the paper, the particle terminal velocity is estimated using the drag coefficient obtained from the mean drag approach. For this purpose, the arithmetic

$$\overline{A_{Parithm}} = \frac{A_{p,\min} + A_{p,\max}}{2}, \tag{11}$$

the geometric

$$\overline{A_{Pgeom}} = \sqrt[2]{A_{p,\min} A_{p,\max}}, \tag{12}$$

and the harmonic mean

$$\overline{A_{Pharm}} = \frac{2 A_{p,\min} A_{p,\max}}{A_{p,\min} + A_{p,\max}}, \tag{13}$$

of $A_{p,\min}$ and $A_{p,\max}$ [m^2] (i.e., the projected areas from the minimum and maximum principal axes of the inertia tensor, respectively) are calculated. After evaluating the above mentioned means (see Sections 3.3 and 4), following Westbrook and Sephton (2017) and McCorquodale and Westbrook (2020), the settling velocity is calculated as:

$$u_{t,sim} = \sqrt{\frac{2gV\Delta\rho}{\rho_{fluid}\overline{C_{D,harm}}\,\overline{A_p}}}, \tag{14}$$

where g is the gravitational acceleration [m/s^2], V is the particle volume [m^3], $\Delta\rho$ is the density difference between the snow crystal and the fluid density [kg/m^3], ρ_{fluid} is the fluid density [kg/m^3], $\overline{C_{D,harm}}$ is the harmonic mean of the drag coefficient from Eq. (9), and $\overline{A_p}$ is the projected area of the particle. A suitable averaged area $\overline{A_p}$ is identified by comparing the calculated terminal velocity with the one measured during laboratory experiments for the same set of particles considered to illustrate the mean drag approach. The respective error is evaluated as:

$$\varepsilon_{u_t} = \frac{u_{t,sim} - u_{t,exp}}{u_{t,sim}} \cdot 100. \tag{15}$$

It is found that the arithmetic mean (Eq. (11)) of the projected areas from the eigenvalues of the inertia tensor gives the best prediction of the particle's terminal velocity. The results are presented in Section 3 and the respective discussion in Section 4.

2.2.2. Turbulence modeling and validation

The flow past an object may create turbulence in the boundary layer and develop a turbulent wake, which generally increases the drag exerted by the flow on the body. In the last decades, Computational Fluid Dynamics (CFD) has played an important role in research related to the study of aerodynamic forces acting on complex-shaped objects. Three main approaches are now available for the computation of turbulent flows: Direct Numerical Simulation (DNS), which provides the most accurate results (no turbulence model is needed) at the highest computational cost, Large-Eddy Simulation (LES) and a statistical approach based on the Reynolds Averaged Navier–Stokes (RANS or URANS for unsteady cases) equations (Pope, 2000; Durbin and Medic, 2007). RANS

models remain widely used in many applications, mainly due to their affordable, low computational cost. However, they present intrinsic difficulties in describing flow around complex-shaped particles, especially because large-scale eddy structures are usually dominant in the flow and unsteady processes like vortex shedding may occur. In these situations, LES approaches are becoming more and more common in the CFD community (Celik, 2003; Davidson, 2020). Large-Eddy Simulations explicitly solve 3D time-dependent Navier-Stokes equations (Eq. (2)) at the larger-scale eddies (resolved grid), while small-scale motions (subgrid), which cannot be resolved on a given grid, are modeled using a filter that splits the domain between the two scales. Since resolving small scales is computationally expensive, LES approaches also overcome the drawbacks of DNS, providing high accuracy at a lower computational cost (Davidson, 2020). In recent years, hybrid RANS-LES modeling strategies (DES - Detached Eddy Simulation) made their way into fluid dynamics research, in particular for bluff body flows. Since LES requires high-resolution grids in near-wall regions, DES solves this issue by combining the best of both RANS and LES: a RANS (URANS) simulation in the viscosity-dominated boundary layer and a LES in the unsteady separated regions (Zhang et al., 2019).

Two different LES and a hybrid URANS-LES models are compared with experimental data (Section 2.1), namely the Smagorinsky model Smagorinsky (1963), WALE Nicoud and Ducros (1999), and DDES Spalart et al. (2006). The latter being an improved version of DES that prevents a too early switch to LES. The DDES model uses the Spalart–Allmaras turbulence closure model for $\tilde{v}$ (modified eddy viscosity) for the RANS calculation, described in details in (Spalart and Allmaras, 1992). Moreover, the model also includes a low Reynolds number correction function in the definition of the length scale (OpenFOAM, 2017; Spalart et al., 2006). In this way, it is possible to cover a much broader range of Reynolds numbers and perform a full validation. To validate these methods, the aggregate particle *AgSt100* is chosen from the given set of snowflakes shown in Fig. 1, in view of the fact that it is the particle with the widest range of Reynolds numbers in the experimental data (Section 2.1 and Table 1), therefore an extensive validation can be carried out. For this, five different *Re* values are solved and the resulting drag coefficient is compared with the experimental value. The error is evaluated using Eq. (10). The averaged absolute error is 8.20% for the Smagorinsky, 6.98% for the WALE, and 6.48% for the DDES, the highest error being for the lowest Reynolds number (*Re* = 38), while at *Re* = 3846 the error reduces consistently in all three tested models. Despite small differences among the performances, the choice falls on the DDES since it proves to be the fastest in terms of computational time. The results of the validation are presented in Table 1 and Fig. 6.

3. Results

The first objective of this work is to predict the drag coefficient of complex-shaped snow particles in air (with Reynolds number range of $50 \lesssim Re \lesssim 2200$) when their final orientation in free-falling motion is known, as described in Section 3.1. Secondly, we propose a new approach to accurately estimate the drag coefficient of snow crystals by employing the same numerical model when the final orientation is not know a posteriori (Section 3.2) and we also present a formula to predict the particle settling velocity and discuss its accuracy.

3.1. Final orientation model

In Fig. 7, the values of the time-averaged drag coefficient (C_D) as a function of Reynolds number are shown for each simulated case (the brackets $\langle \rangle$ are dropped from now on for simplicity).

The drag coefficients calculated from the computational model are compared with experimental values, displayed with their uncertainty ($\pm 7\%$). A strong dependency of the prediction accuracy on the particle falling motion (steady, periodic or chaotic) is observed: for particles that fell steadily for the entire simulated *Re* range (*D1007* and *CR512*), the averaged absolute error falls within the measurements uncertainty interval ($\pm 7\%$) being 2.75% and 5.09% for *D1007* and *CR512*, respectively. At low Reynolds numbers ($Re \lesssim 250$), almost all the particles show a steady falling behavior during experiments. For these cases the model prediction errors fall again within the experimental uncertainty. The only exception is the rosette crystal *MR172*, which fell with a periodic motion already at *Re* = 184 and for which the model slightly overpredicts the drag coefficient with an error of 12.59%. At low Reynolds number, particles with lower area ratio A_R (e.g., plate-like particle) tend to exhibit higher C_D, while for $Re \gtrsim 250$ this aspect is less pronounced (except for the plate-like crystal *D1007*), as shown in Fig. 8. Fig. 8(a) depicts the results for Reynolds numbers lower than approximately 250, for which the errors in the drag coefficient estimate fall generally below the experimental uncertainty ($\pm 7\%$).

A substantial difference in the drag prediction between snow particles is instead observable at higher Reynolds numbers ($Re \gtrsim 250$). For aggregates (*AgCr77, Ag15P1*, and *AgSt18*), even if these geometries manifest a periodic motion above $Re \gtrsim 1000$ (Section 2.1.1), the drag coefficient is still well predicted, with the largest absolute error being 10.60% for *Ag15P1* at *Re* = 2049 (Table 2). In contrast, for *CC20Hex2* and *MR172*, which showed periodic/chaotic behavior at moderately high Reynolds numbers, the errors in the drag estimate are much larger. *CC20Hex2* displays a general overestimation of C_D with a largest absolute error of 40.63% for *Re* = 858, while *MR172* carries much larger differences with the experimental data and a general underestimation of the drag (largest absolute error being 49.74% for *Re* = 1385). The weakness of the final orientation model in predicting the drag coefficient in case of chaotic motion (*CC20Hex2, MR172*) is clearly visible in Fig. 8(b), which also collects the estimated error for all the other cases at $Re \gtrsim 250$. Larger errors are also observed for particles with area ratio $A_R \gtrsim 0.5$ (*CC20Hex2* and *MR172*), particularly for $Re \gtrsim 250$. In Table 2, all the computational and experimental results are listed for completeness, together with the area ratio values for each particle.

The errors for *CC20Hex2* increase from 6.95% (comparable to experimental uncertainty) to 33.56% between *Re* = 59 and *Re* = 251, which correlates with a radical change in its fall motion. At *Re* = 59, the particle falls steadily with the column element positioned horizontally. At *Re* = 251, the particle falls unsteadily, oscillating periodically around an orientation where the column is vertical. As *Re* increases further, the motion becomes chaotic, and the errors become even larger (40.63% at *Re* = 858). Similar behavior is evident in the data for *MR172*. At *Re* = 62, where the particle falls steadily, the error is only 6.11%. Increasing *Re* further leads to chaotic motions and larger errors (49.74% at *Re* = 1385). Based on this evidence, we argue that the large discrepancies between model and experiments, especially at $Re \gtrsim 250$, are ascribable to large-amplitude oscillations during chaotic motion. In these cases, in fact, the variation of the frontal area of the particle concerning the flow direction is more pronounced. Therefore, the assumption that the orientation we observed when particles fell steadily can be considered representative of an "average" orientation for particles that fall unsteadily, becomes unreliable. As a consequence, the final orientation model is not suitable anymore for cases in which the particle falls with a chaotic motion at high Reynolds numbers. This is a reason to look for a more general approach that accurately estimates the drag coefficient of complex-shaped particles, as described in Section 3.2.
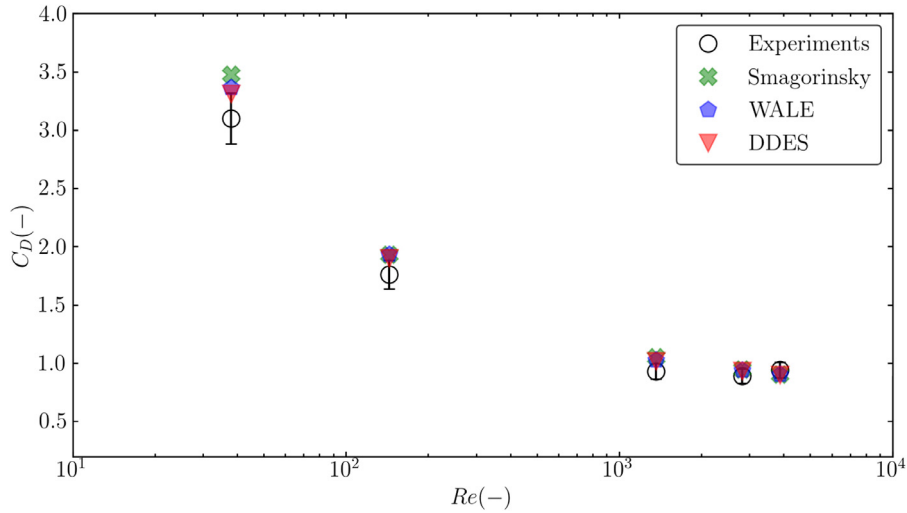
Fig. 6. Results from the validation (particle *AgSt100*) for the time-averaged drag coefficient prediction (⟨⟩ dropped for simplicity) using two different LES models (Smagorinsky and WALE) and a DDES (hybrid URANS-LES) model. The average error for the Smagorinsky, WALE, and DDES approach is 8.20%, 6.98%, and 6.48%, respectively. Laboratory data uncertainty is ±7%.

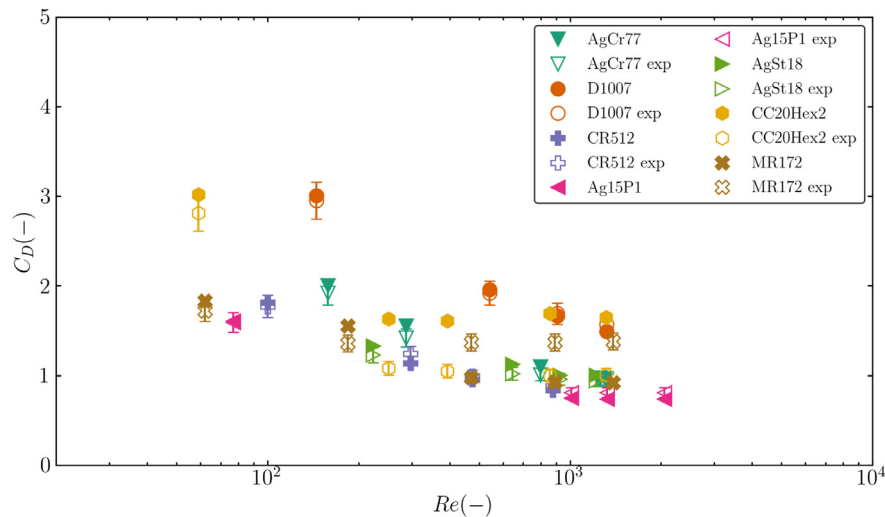**Fig. 7.** Time-averaged drag coefficient comparison (⟨⟩ dropped for simplicity) between the model and experimental data (uncertainties of experimental data ±7%).

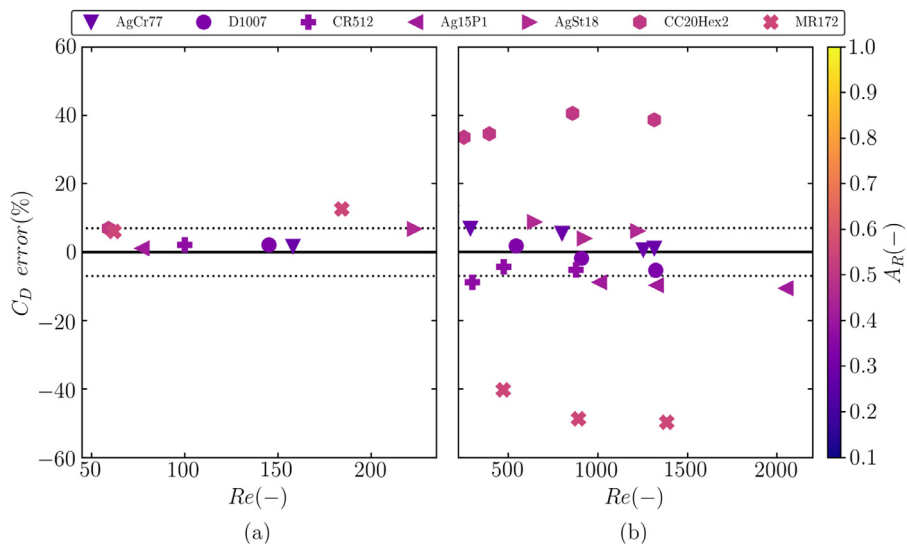**Fig. 8.** Drag coefficient prediction errors of the model for (a) $50 \lesssim Re \lesssim 250$ and (b) $250 \lesssim Re \lesssim 2200$. The zero line represents the reference values, i.e., experimental data. The dotted lines are the uncertainties in the experimental measurements (±7%). The different colors indicate the area ratio A_R for each particle, whose range is given in the color bar on the right.
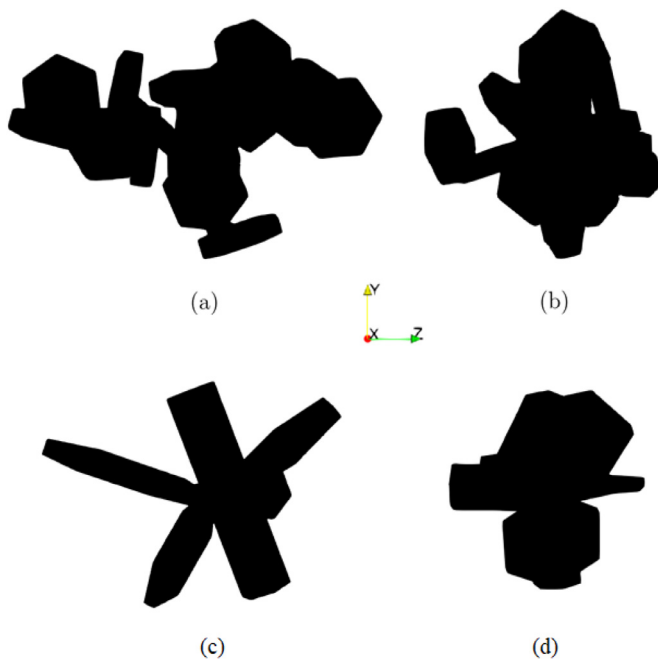
Fig. 9. Projected areas corresponding to the maximum (a, c) and minimum (b, d) principal moment of inertia of particles *Ag15P1* (a, b) and *MR172* (c, d). The flow direction coincides with the *x* axis.

3.2. Drag coefficient estimate from arithmetic, geometric and harmonic mean

The second part of this work illustrates a systematic approach to evaluate the drag coefficient of irregular particles using our numerical model, when the final orientation is not known.

From the eigenvalues of the inertia tensor of an object it is possible to identify the maximum and minimum principal moment of inertia and their correspondent projected areas (these projected areas are not necessarily the particle maximum and minimum projected areas normal to the flow, among all the possible orientations). This calculation was performed on the STL files of the snow particles *AgCr77, Ag15P1, MR172* and *CC20Hex2*. These four particles are chosen among all the simulated ones because they are representative of cases in which periodic or chaotic motion was observed during experiments, i.e., for which it is more difficult to define an unequivocal final orientation. For each particle, only three Reynolds number are chosen for demonstration purposes, namely $Re = 158, 799, 1314$, $Re = 77, 1009, 2049$, $Re = 251, 858, 1315$, $Re = 472, 890, 1385$ for *AgCr77, Ag15P1, CC20Hex2*, and *MR172*, respectively. The projected areas corresponding to the maximum and minimum principal moments of inertia of *Ag15P1* and *MR172* are shown in Fig. 9. A set of two simulations (one for each projected area) for each snowflake is thus built for each Reynolds number, according to Section 2.2. Pairs of $\langle C_{D,\min} \rangle$ and $\langle C_{D,\max} \rangle$ are acquired at different flow regimes and the arithmetic, geometric, and harmonic means are evaluated using Eqs. (7)–(9), respectively.

Fig. 10 depicts the final orientation's errors and the different means with the experimental data as reference. The large difference between the final orientation model and the different means in the drag coefficient estimate is clearly visible. Aggregates (*AgCr77* and *Ag15P1*) present a slight improvement in the prediction of the drag coefficient with the adoption of the harmonic mean. The averaged absolute error goes from 2.80% and 6.81% for the final orientation model to 1.22% and 4.48% for *AgCr77* and *Ag15P1*, respectively (see Table 3). For the columnar crystal *CC20Hex2* and the rosette *MR172*, the harmonic mean show a sig-

nificant improvement in the prediction compared to the final orientation model. The averaged absolute error drops from 37.76% and 46.28% to 4.79% and 7.44% for *CC20Hex2* and *MR172*, respectively.

This novel approach takes advantage of the eigenvalues of the inertia tensor to extract the projected areas corresponding to the maximum and minimum principal moment of inertia of a particle to obtained $\langle C_{D,\min} \rangle$, $\langle C_{D,\max} \rangle$. From these values, a mean drag is calculated using the harmonic mean, that provides a better estimate of C_D than the final orientation approach when falling behavior is not stable. Therefore, it can be used to evaluate the drag coefficient of complex-shaped particles that fall with both stable and unstable behavior, without requiring a posteriori knowledge of the kinematics of the particle.

3.3. Evaluation of snow particles terminal velocity

For the evaluation of the snowflakes terminal velocities, Eq. (14) is used. $A_{p,arith}$ is identified as the most suitable area by comparing the terminal velocity calculated with Eq. (14) for different mean areas (Eqs. (11)–(13)) with the settling velocity from experimental data, evaluating the errors according to Eq. (15). The results are shown in Table 5 and include the particles considered for the mean drag approach. From the table, one can see that for all the tested particles, the area measured during experiments gives the lowest averaged absolute error for the settling velocity prediction. However, measuring the area of such particles during their free-fall is a very difficult task and not always achievable. Consequently, the arithmetic mean of the projected areas ($A_{p,arithm}$) is chosen. Compared to the other means, it displays the lowest value for all the geometries except from *MR172*, for which the harmonic mean offers a slightly better performance. However, since for *MR172* the difference between the error of $A_{p,harm}$ and $A_{p,arithm}$ is $\approx 1\%$, the arithmetic mean can be employed in Eq. (14) without introducing larger errors. The errors related to the terminal velocity prediction fall within the uncertainties of previous models in literature (Mitchell and Heymsfield, 2005; Heymsfield and Westbrook, 2010). The choice of the area for the terminal velocity prediction is further discussed in Section 4.

4. Discussion

Experimental and numerical approaches have been employed to investigate the falling behavior of fairly simple geometries (such as disks Auguste et al. (2013); Sanjeevi et al. (2018), cylinders Toupoint et al. (2019), planar polygons Esteban et al. (2019), and plate-like particles Cheng et al. (2015); Nedic et al. (2013) and to identify the causes of the onset of unsteady behavior concerning geometrical features of falling objects (Auguste et al., 2013; Vincent et al., 2016). Although these studies shed some light on the falling behavior, they are limited by less complex shapes and narrower Reynolds number ranges ($Re \lesssim 100$). In this view, the final orientation model provides an accurate prediction of the drag coefficient of complex-shaped particles when they fall steadily or with periodic motion. It can also be used to identify a more suitable shape factor to improve models parametrizations. In this paper, only the dependency on A_R is shown for consistency with the work of McCorquodale and Westbrook (2020), but further investigation is needed for what concerns shape factors. As shown in Section 3.1, for $A_R \gtrsim 0.5$ the final orientation model shows a drop in accuracy, which can be explained by the fact that particles with larger A_R (such as *CC20Hex2* and *MR172*) display unsteady falling behavior already at $Re \gtrsim 100$ (Fig. 2). This exposes the model limitations directly associated with the uncertainties in defining a representative "final orientation", particularly for particles that exhibit chaotic motion at high Re, which manifests as a dependence of the
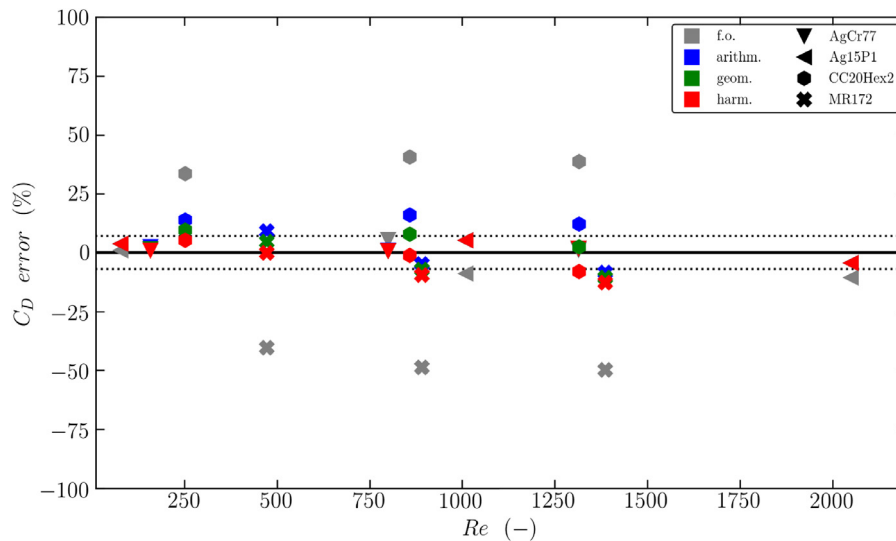
Fig. 10. Comparison between mean drag coefficients evaluated with arithmetic (blue), geometric (green), and harmonic mean (red), and drag coefficients from simulations with the particles at their final orientations (grey). The zero line represents the reference values, i.e., experimental data. The dotted lines are the uncertainties in the experimental measurements ($\pm 7\%$). (For interpretation of the references to color in this figure legend, the reader is referred to the web version of this article.)

Table 4
Comparison between absolute average errors of the drag coefficient estimate from the final orientation model, the mean drag approach, and two different models for irregular particles taken from the literature.

	Averaged absolute error (%)			
Particle	Final orientation	Harmonic mean	Hölzer and Sommerfeld (2008)	Dioguardi et al. (2018)
AgCr77	2.80	1.22	48.21	63.27
Ag15P1	6.81	4.48	58.97	75.56
CC20Hex2	37.76	4.79	55.04	48.59
MR172	46.28	7.44	37.29	58.99

Table 5
Averaged absolute error of the snow particle settling velocity evaluated with different means of the maximum and minimum projected area from the eigenvalues of the inertia tensor (Eqs. (11)–(13)) and with the projected areas from the experiments (A_{exp}). u_t is evaluated using Eq. (14), while the error ε_{u_t} with Eq. (15).

	Settling velocity averaged absolute error (%)			
	$\varepsilon_{u_t} A_{arithm}$	$\varepsilon_{u_t} A_{geom}$	$\varepsilon_{u_t} A_{harm}$	$\varepsilon_{u_t} A_{exp}$
AgCr77	23.75	26.54	29.22	18.75
Ag15P1	24.13	24.38	24.62	22.17
CC20Hex2	16.36	17.92	29.51	15.24
MR172	16.34	15.89	15.43	12.66

simulation accuracy on the falling behavior for the final orientation approach.

Extensive work has been done on the drag coefficient for spherical particles (Abraham, 1970; Clift et al., 1978), ellipsoids Oseen (1927); Sanjeevi et al. (2018) and disks (Field et al., 1997). For irregular particles, the tendency has always been to propose models based on parameters that quantify the particle shape (Bagheri and Bonadonna, 2016; Mitchell and Heymsfield, 2005; Heymsfield and Westbrook, 2010). These models perform quite well at low Reynolds numbers ($Re \lesssim 100$), but become less accurate as Re increases. Furthermore, previously proposed models (Hölzer and Sommerfeld, 2008; Dioguardi et al., 2018; Mitchell and Heymsfield, 2005) suffer from the intrinsic difficulty of defining a unique shape factor that describes the particle behavior for a large variety of flow regimes. This is also shown in the comparison of Table 4, in which the averaged absolute error of the drag coefficient (over the Reynolds number range of the mean drag approach)

evaluated with two different models from literature (Hölzer and Sommerfeld, 2008; Dioguardi et al., 2018) is compared with the final orientation model and the harmonic mean approach. Large errors ($\gtrsim 50\%$) are present for both literature models. This is expected to some extent since the geometries considered in those works have simpler shapes than snowflakes and the parametrization is based solely upon sphericity.

To overcome the drawbacks of the final orientation model and of parametrizations found in literature, the mean drag approach is presented. The latter relies on the projected areas derived from the minimum and maximum eigenvalues of the particle inertia tensor. As a result, it is not dependent on the final orientation reconstruction; thereby, its accuracy is not limited by A_R or by the snowflake falling behavior. Therefore, this approach can be used to investigate the aerodynamic response of ice particles for which no corroborating data is available. To test the efficiency and the large applicability of this approach, the geometries *AgCr77, Ag15P1, CC20Hex2*, and *MR172* were chosen among the ones that exhibited periodic or chaotic motion. The results discussed in Section 3.2 present the mean drag approach with the harmonic mean as a reliable alternative to predict the drag coefficient of irregular particles, especially at high Reynolds numbers, for which the final orientation model or other parametrized models perform poorly (Table 4). To better illustrate why the mean drag approach works, the projected areas (Fig. 11) and the drag coefficients (Fig. 12) from the experiments, the final orientation and the minimum and maximum eigenvalues models are compared. From Fig. 11, it emerges that for almost all particles the projected area of the final orientation is comparable to the average projected area measured during experiments, while the projected areas of the minimum and the maximum eigenvalues slightly (for aggregates) or considerably (for *MR172*) differ from
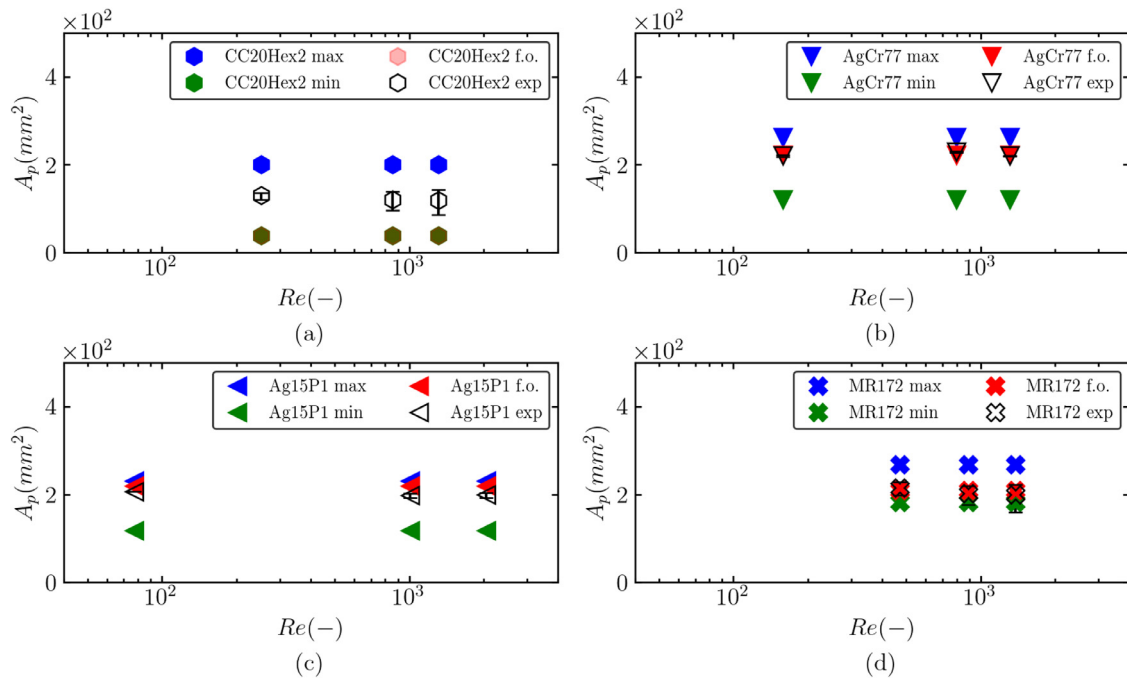
Fig. 11. Comparison between the projected areas of experiments (exp), final orientation model (f.o.), maximum (max) and minimum (min) eigenvalues projected area approach for particles (a) *CC20Hex2*, (b) *AgCr77*, (c) *Ag15P1*, and (d) *MR172*. For the capped-column *CC20Hex2*, the final orientation and the minimum eigenvalue projected areas coincide.
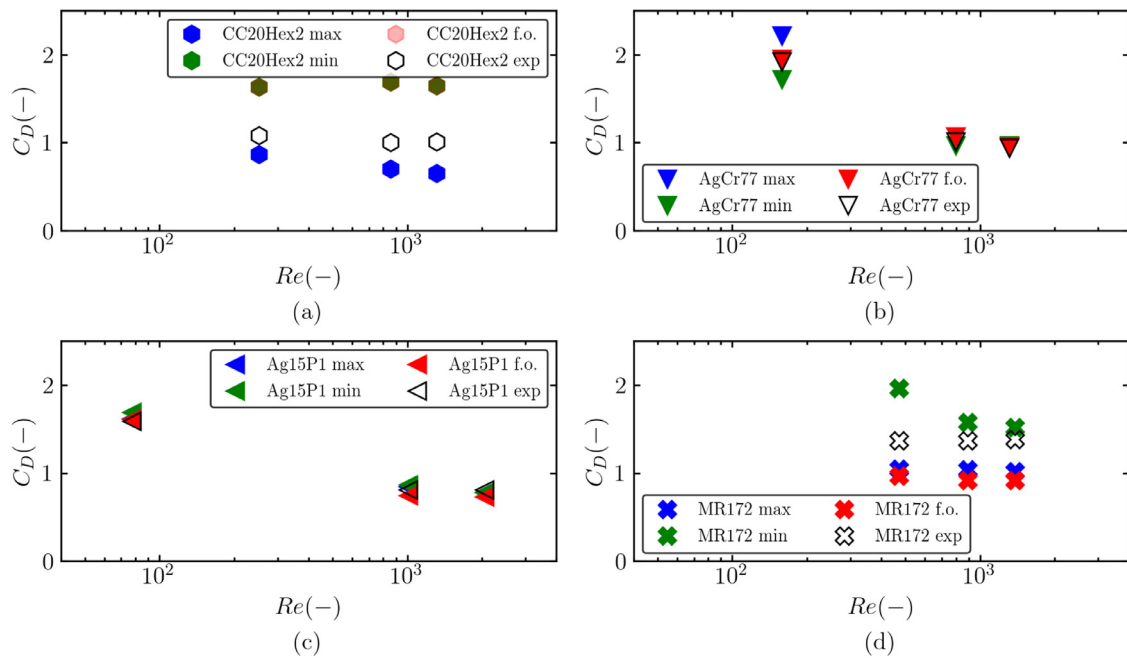

Fig. 12. Comparison between the drag coefficient evaluated from experiments (exp), final orientation model (f.o.), maximum (max) and minimum (min) eigenvalues projected area approach for particles (a) *CC20Hex2*, (b) *AgCr77*, (c) *Ag15P1*, and (d) *MR172*. For the capped-column *CC20Hex2*, the drag of the final orientation model and the minimum eigenvalue one coincide, since the particle orientation (and thus the projected areas) are the same.

the laboratory measurements. This is not the case for *CC20Hex2*, for which the areas from the final orientation and the minimum eigenvalue projected area models coincide. The final orientation of each geometry originates from the assumption that the orientation observed when the particle fall steadily lies within the range of the positions adopted during unsteady falling motion. In Fig. 11 (a), it is evident that this assumption is not valid for *CC20Hex2*, which displayed chaotic motion for the simulated *Re*. The final orientation model does not perform well, as the error for *CC20Hex2* becomes

large at the point where the orientation of the particle changes by 90° and becomes unsteady. To find an explanation on why the final orientation model is not suitable for *MR172*, we need to look at Fig. 12 (d). While for this particle the areas do not differ much, the drag coefficient of the final orientation seems to be at a local minimum. This is probably a consequence of the sharp change in the drag coefficient as the particle rotates in the vicinity of its "final orientation". Figs. 11 and 12 show that the mean drag approach gives us some rough estimate of the maximum and minimum pos-

Table 6
Errors of the mean areas evaluated with Eqs. (11)–(13) in comparison with the projected areas measured from the experiments.

Re	Error (%)		
	A_{arith}	A_{geom}	A_{harm}
AgCr77			
158	13.18	19.55	25.45
799	16.96	23.04	28.70
1314	13.18	19.55	25.45
averaged absolute error	14.44	20.71	26.53
Ag15P1			
77	15.53	19.90	24.27
1009	11.68	16.24	20.81
2049	12.56	17.09	21.61
averaged absolute error	13.26	17.74	22.23
CC20Hex2			
251	7.69	32.31	50.00
858	0.00	26.67	45.83
1315	−0.84	26.05	45.38
averaged absolute error	2.84	28.34	47.07
MR172			
472	−4.17	−2.31	−0.46
890	−10.84	−8.87	−6.90
1385	−12.50	−10.50	−8.50
averaged absolute error	9.17	7.23	5.29

sible drag coefficients for each particle (from all its possible orientations), and then by averaging them with the harmonic mean, we get closer to the value of its real final orientation. These plots also show that the real particle behavior is much more complicated because some particles present a strong dependency of the drag on their final orientation, whilst for others this influence is less pronounced (aggregates). Table 4 also highlights that the current mean drag approach yields significantly smaller errors in drag prediction. In this study, we considered simple shapes, such as the dendrite plate, as well as more complex, irregular geometries. In particular, during experiments we observed that the dendrite particle exhibits broadly similar kinematics to a circular disc (for example they both orientate with the largest area perpendicular to the fall direction) and so we expect the model to be valid also for other simple shapes.

An estimate of the terminal velocity of the same set of snow particles used for the mean drag approach is given by Eq. (14). In the latter, $\overline{A_p}$ is identified as the arithmetic mean of the maximum and minimum projected areas from the eigenvalues of the inertia tensor (Eq. (11)). As already mentioned in Section 3.3, the areas measured during the laboratory tests display the lowest errors (Table 5). However, measuring the area of complex-shaped ice crystals is generally unfeasible. Therefore, among different tested means (Eqs. (11)–(13)), the arithmetic mean of the areas is chosen (Eq. (11)). This choice yields prediction errors within the range of accuracy of previous models in literature (Mitchell and Heymsfield, 2005; Heymsfield and Westbrook, 2010). To justify our choice, the errors between the projected area measured for each particles during the experiments and the means evaluated using Eqs. (11)–(13) are reported in Table 6. For all the tested particles, the error between the experimental area and the arithmetic mean of the areas from the inertia tensor falls below $\approx 17\%$, the lowest among the compared values. The only particles that shows a different tendency is *MR172*, for which the harmonic mean gives a slightly better performance. To explain this, we need to look at Fig. 11, in which it is evident that the experimental area of particle *MR172* tends to be closer to the smallest area extracted from the inertia tensor, due to the particle chaotic motion. In addition, the harmonic mean leans towards the smallest values. This is consistent with the particle's behavior (Fig. 11) and explains why the harmonic mean yields lower errors for this geometry. On the other

hand, the arithmetic mean favors the largest values and can than be related to the particle general tendency towards the lowest drag coefficient (i.e., the largest projected area). This behavior justifies the use of the arithmetic mean of the areas to evaluate the settling velocity. For *MR172*, the averaged absolute error between harmonic and arithmetic mean remains $\lesssim 1\%$ and hence the latter can be considered also for this particle, without introducing large errors in the settling velocity prediction.

5. Conclusions

The objective of this work was twofold: to present a DDES model to predict the drag coefficient of complex-shaped snow particles in air beyond the Stokes regime when their final orientation during free-falling is known, and to describe a systematic approach for the drag estimate when the final orientation is unknown a posteriori, employing the same computational set-up and the eigenvalues of the inertia tensor. The model's potential was demonstrated using a set of geometries representing the main snowflakes classes to render the model as widely applicable as possible.

The final orientation model was informed by experiments with 3D-printed analogs falling in a water-glycerin and the simulations results were compared with experimental data to assess the model accuracy. At $Re \lesssim 250$, almost all the geometries showed steady falling motion during laboratory tests, and the model prediction errors fell within the experimental uncertainty ($\pm 7\%$). The only exception was the rosette crystal (*MR172*), for which periodic motion is already present at $Re = 184$, and thus resulted in a slightly poorer prediction. At moderately high Reynolds numbers ($250 \lesssim Re \lesssim 2200$), the prediction errors remained below 10% for particles with steady and periodic motion. However, the model failed to predict the drag coefficient for snowflakes with chaotic motion, yielding errors larger than $\approx 30\%$. A general dependency of the estimate accuracy on the snow particles' falling motion was observed, together with a lower accuracy for particles with area ratio larger than 0.5. The latter dependency still needs to be further investigated. The final orientation model provides a reasonably accurate prediction of the drag coefficient of markedly irregular particles with steady or periodic falling motion and may help gain insights on the particle behavior in relation to the changes in the wake structure (Fernandes et al., 2007). The model also elucidates how 3-dimensional geometric features influence the onset of unsteady motion Auguste et al. (2013), which need to be further investigated and will be the objectives of future steps of this work.

To overcome the difficulties in the estimate of the drag coefficient for particles with chaotic falling behavior a novel, systematic approach was proposed. From the eigenvalues of the inertia tensor of each snow crystal, the projected areas corresponding to the maximum and minimum principal moment of inertia were identified and used in the DDES model to obtain pairs of drag coefficients matching the Reynolds numbers of the experiments. From these pairs of values, the arithmetic, geometric, and harmonic mean were calculated and compared with experimental values. The harmonic mean gives the most accurate estimate of the drag coefficient (within the experimental uncertainty) for a diverse range of snowflakes geometries and provides much better predictions than empirical correlations based on simpler shapes.

Regarding the particles settling velocity, we found a satisfying prediction using Eq. (14), in which we used the harmonic mean of the drag coefficient and the arithmetic mean of the areas obtained from the eigenvalues of the inertia tensor. The accuracy of the proposed formula for the terminal velocity lies within the one exhibited by other models in literature.

The DDES model presented in this work, combined with the new approach based on the mean drag, is a reliable tool to predict the drag coefficient from irregular snow particles falling in air and constitute a less computationally expensive solution than a 6DoF solver or DNS codes. This novel approach is also not dependent on the final orientation reconstruction and thus can be used to investigate the drag coefficient of snowflakes for which no extensive data on orientation are available. Additionally, it represents an important step towards a much deeper understanding of the drag dependence on shape parameters and wake structure, and a valuable tool to investigate the falling motion of complex-shaped particles in different types of industrial processes and environmental phenomena.

Declaration of Competing Interest

The authors declare that they have no known competing financial interests or personal relationships that could have appeared to influence the work reported in this paper.

CRediT authorship contribution statement

Giorgia Tagliavini: Conceptualization, Data curation, Investigation, Methodology, Software, Supervision, Validation, Writing - original draft, Writing - review & editing. **Mark McCorquodale:** Data curation, Methodology, Supervision, Validation, Writing - review & editing. **Chris Westbrook:** Data curation, Supervision, Writing - review & editing. **Pascal Corso:** Methodology, Software, Writing - review & editing. **Quirine Krol:** Conceptualization, Writing - review & editing. **Markus Holzner:** Conceptualization, Supervision, Writing - review & editing.

Acknowledgments

Supplementary material

Supplementary material associated with this article can be found, in the online version, at 10.1016/j.ijmultiphaseflow.2021.103652

References

Abraham, F.F., 1970. Functional dependence of drag coefficient of a sphere on Reynolds number. Phys. Fluids 13, 2194–2195.

Auguste, F., Magnaudet, J., Fabre, D., 2013. Falling styles of disks. J. Fluid Mech. 719, 388–405.

Bagheri, G., Bonadonna, C., 2016. On the drag of freely falling non-spherical particles. Powder Technol. 301, 526–544.

Binder, C., Feichtinger, C., Schmid, H.J., Thürey, N., Peukert, W., Rüde, U., 2006. Simulation of the hydrodynamic drag of aggregated particles. J. Colloid Interface Sci. 301, 155–167.

Brady, J., Bossis, G., 1988. Stokesian dynamics. Annu. Rev. Fluid Mech. 20, 111–157.

Brenner, H., 1963. The Stokes resistance of an arbitrary particle. Chem. Eng. Sci. 18, 1–25.

Celik, I., 2003. RANS/LES/DES/DNS: the future prospects of turbulence modeling. J. Fluids Eng. 127, 829–830.

Cheng, K.Y., Wang, P.K., Hashino, T., 2015. A numerical study on the attitudes and aerodynamics of freely falling hexagonal ice plates. J. Atmos. Sci. 72, 3685–33698.

Davidson, L., 2020. Fluid mechanics, turbulent flow and turbulence modeling.

Clift, R., Grace, J. R., Weber, M. E., 1978. Bubbles, Drops and Particles. Dover Publications.

Dawson-Haggerty, et al., 2019. trimesh. https://trimsh.org/

Dioguardi, F., Mele, D., Dellino, P., 2018. A new one-equation model of fluid drag for irregularly shaped particles valid over a wide range of Reynolds number. J. Geophys. Res. 123 (1), 144–156.

Durbin, P.A., Medic, G., 2007. Fluid Dynamics with a Computational Perspective. Cambridge University Press.

Esteban, L.B., Shrimpton, J., Ganapathisubramani, B., 2019. Three dimensional wakes of freely falling planar polygons. Exp. Fluids 60 (114).

Fernandes, P.C., Risso, F., Magnaudet, J., 2007. Oscillatory motion and wake instability of freely rising axisymmetric bodies. J. Fluid Mech. 573, 2625–2633.

Ferziger, J.H., Perić, M., 2002. Computational Methods for Fluid Dynamics. Springer.

Field, S., Moore, M.G., Nori, F., 1997. Chaotic dynamics of falling disks. Nature 388, 252–254.

Franke, J., Hellsten, A., Schlünzen, H., Carissimo, B., 2007. Best practice guideline for the CFD simulation of flows in the urban environment. COST Action 732.

Garrett, T.J., Fallgater, C., Shkurko, K., Howlett, D., 2012. Fall speed measurement and high-resolution multi-angle photography of hydrometeors in free fall. Atmos. Meas. Tech. 5, 2625–2633.

Gunn, K.L.S., Marshall, J.S., 1957. The distribution with size of aggregate snowflakes. J. Meteorol. 15, 452–461.

Happel, J., Brenner, H., 1983. Low Reynolds Number Hydrodynamics, 1. Special Applications to Particulate Media.

Hashino, T., Cheng, K.Y., Chueh, C.C., Wang, P.K., 2016. Numerical study of motion and stability of falling columnar crystals. J. Atmos. Sci. 73, 1923–1942.

Heymsfield, A.J., Westbrook, C.D., 2010. Advances in the estimation of ice particle fall speeds using laboratory and field measurements. J. Atmos. Sci. 67, 2469–2482.

Hölzer, A., Sommerfeld, M., 2008. New simple correlation formula for the drag coefficient of non-spherical particles. Powder Technol. 184, 361–365.

Kikuchi, K., Kameda, T., Higuchi, K., Yamasita, A., 2013. A global classification of snow crystals, ice crystals, and solid precipitation based on observations from middle latitudes to polar regions. Atmos. Res. 132, 460–472.

Kim, T., Chang, J., Kim, D., 2018. Free-fall dynamics of a pair of rigidly linked disks. Phys. Fluids 30, 034104.

Langleben, M.P., 1954. The terminal velocity of snowflakes. Q. J. R. Meteorol. Soc. 80, 174–181.

Leith, D., 1987. Drag of nonspherical objects. Aerosol Sci. Technol. 6, 153–161.

List, R., Schemenauer, R.S., 1971. Free-fall behaviour of planar snow crystals, conical graupel and small hail. J. Atmos. Sci. 28, 110–115.

Magono, C., Nakamura, T., 1965. Aerodynamic studies of falling snowflakes. J. Meteorol. Soc. Jpn. 43, 139–147.

McCorquodale, M. W., Westbrook, C. D., 2020. TRAIL: a Novel Experimental Approach for Studying the Aerodynamics of Ice Particles. Quarterly Journal of the Royal Meteorological Society.

McCorquodale, M. W., Westbrook, C. D., 2020. TRAIL part 2: a Comprehensive Assessment of Ice Particle Fall Speed Parametrisations. Quarterly Journal of the Royal Meteorological Society.

Mitchell, D.L., Heymsfield, A.J., 2005. Refinements in the treatment of ice particle terminal velocities, highlighting aggregates. J. Atmos. Sci. 62, 1637–1644.

Moukalled, F., Mangani, L., Darwish, M., 2016. The finite volume method in computational fluid dynamics : an advanced introduction with OpenFOAM and Matlab. Springer.

Nedic, J., Ganapathisubramani, B., Vassilicos, J.C., 2013. Drag and near wake characteristics of flat plates normal to the flow with fractal edge geometires. Fluid Dyna. Res. 45, 061406.

Newman, A.J., Kucera, P.A., Bliven, L.F., 2009. Presenting the snowflake video imager (SVI). J. Atmos. Ocean. Technol. 26, 167–179.

Nicoud, F., Ducros, F., 1999. Subgrid-scale stress modelling based on the square of the velocity gradient tensor. Flow Turbul. Combust. 62, 183–200.

OpenFOAM, 2017. User Guide - OpenFOAM 5.0.

Oseen, C. W., 1927. Hydrodynamik.

Ouchene, R., Khalij, M., Arcen, B., Tanière, A., 2016. A new set of correlations of drag, lift and torque coefficients for non-spherical particles and large Reynolds numbers. Powder Technol. 303, 33–43.

Pope, S.B., 2000. Turbulent Flows. Cambridge University Press.

Proudman, I., Pearson, J. R. A., 1957. Expansions at small Reynolds numbers for the flow past a sphere and a circular cylinder. Journal of Fluid Mechanics 2, 237–262.

Roache, P.J., 1994. Perspective: a method for uniform reporting of grid refinement studies. J. Fluids Eng. 116 (3), 405–413.

Sanjeevi, S.K.P., Kuipers, J.A.M., Padding, J.T., 2018. Drag, lift and torque correlations for non-spherical particles from stokes limit to high Reynolds numbers 106, 325–337.

Schönhuber, M., Lammer, G., Randeu, W., 2007. One decade of imaging precipitation measurement by 2D-video distrometer. Adv. Geosci. 10, 85–90.

Smagorinsky, J., 1963. General circulation experiments with the primitive equations I. The basic experiment. Mon. Weather Rev. 91, 99–164.

Spalart, P., Allmaras, S., 1992. A one-equation turbulence model for aerodynamic flows. In: AIAA Paper, pp. 92–439.

Spalart, P.R., Deck, S., Shur, M.L., Squires, K.D., Strelets, M.K., Travin, A., 2006. A new version of detached-eddy simulation, resistant to ambiguous grid densities. Theor. Comput. Fluid Dyn. 20, 180.

Stokes, G.G., 1851. On the effect of the internal friction of fluids on the motion of pendulums. Trans. Cambridge Philos. Soc. 9, 1–8.

Toupoint, C., Ern, P., Roig, V., 2019. Kinematics and wake of freely falling cylinders at moderate Reynolds numbers. J. Fluid Mech. 866, 21–32.

Tran-Cong, S., Gay, M., Michaelides, E.E., 2004. Drag coefficients of irregularly shaped particles. Powder Technol. 139, 82–111.

Uhlmann, M., Dusek, J., 2014. The motion of a single heavy sphere in ambient fluid: a benchmark for interface-resolved particulate flow simulations with significant relative velocities. Int. J. Multiph. Flow 50, 221–243.

Vincent, L., Shambaugh, W., Kanso, E., 2016. Holes stabilize freely falling coins. J. Fluid Mech. 801, 250–259.

Westbrook, C.D., 2008. The fall speeds of sub-100 microns ice crystals. Q. J. R. Meteorol. Soc. 134, 1243–1251.

Westbrook, C.D., Sephton, E.K., 2017. Using 3D-printed analogues to investigate the fall speeds and orientations of complex ice particles. Geophys. Res. Lett. 44, 7994–8001.

Zastawny, M., Mallouppas, G., Zhao, F., van Wachem, B., 2012. Derivation of drag and lift force and torque coefficients for non-spherical particles in flows. Int. J. Multiph. Flow 39, 227–239.

Zeugin, T., Krol, Q., Fouxon, I., Holzner, M., 2020. Sedimentation of snow particles in still air in stokes regime. Geophys. Res. Lett. 47 (15), e2020GL087832.

Zhang, C., Bounds, C., Foster, L., Uddin, M., 2019. Turbulence modeling effects on the CFD predictions of flow over a detailed full-scale sedan vehicle. Fluids 4, 148.